Quantum-limited optical time transfer for future geosynchronous links

https://doi.org/10.1038/s41586-023-06032-5

Received: 15 December 2022

Accepted: 30 March 2023

Published online: 21 June 2023



Check for updates

Emily D. Caldwell^{1,2,5}, Jean-Daniel Deschenes^{3,5}, Jennifer Ellis¹, William C. Swann¹, Benjamin K. Stuhl⁴, Hugo Bergeron³, Nathan R. Newbury^{1,5™} & Laura C. Sinclair^{1,5™}

The combination of optical time transfer and optical clocks opens up the possibility of large-scale free-space networks that connect both ground-based optical clocks and future space-based optical clocks. Such networks promise better tests of general relativity¹⁻³, dark-matter searches⁴ and gravitational-wave detection⁵. The ability to connect optical clocks to a distant satellite could enable space-based very long baseline interferometry^{6,7}, advanced satellite navigation⁸, clock-based geodesy^{2,9,10} and thousandfold improvements in intercontinental time dissemination^{11,12}. Thus far, only optical clocks have pushed towards quantum-limited performance¹³. By contrast, optical time transfer has not operated at the analogous quantum limit set by the number of received photons. Here we demonstrate time transfer with near quantum-limited acquisition and timing at 10,000 times lower received power than previous approaches $^{14-24}$. Over 300 km between mountaintops in Hawaii with launched powers as low as 40 µW, distant sites are synchronized to 320 attoseconds. This nearly quantum-limited operation is critical for long-distance free-space links in which photons are few and amplification costly: at 4.0 mW transmit power, this approach can support 102 dB link loss, more than sufficient for future time transfer to geosynchronous orbits.

Comb-based optical time transfer (OTT) follows previous microwave two-way time-frequency transfer²⁵. Optical pulses from coherent frequency combs located at remote sites are exchanged across a two-way free-space link. The difference in the detected pulse time-of-arrival between sites yields their clock offset, independent of the time-of-flight (assuming full reciprocality). Previous comb-based OTT used linear optical sampling (LOS) against a local frequency comb with an offset repetition rate to scan across the incoming comb pulses and measure their timing¹⁴⁻²⁴. This approach is photon inefficient and requires signals of a few nanowatts, 40 dB above the quantum limit. Despite this, with a combination of 40-cm aperture telescopes, adaptive optics and watt-level amplifiers, Shen et al. 24 achieved a working range of 113 km. The alternative approach of conventional optical frequency transfer (OFT) using continuous wave lasers achieves high performance^{26–28} but is unable to measure the elapsed time between sites—the quantity of interest to many applications-in the presence of link disruption due to atmospheric turbulence, weather or multiplexed operation.

In close analogy with optical clocks, the quantum-limited uncertainty for time transfer by means of an optical pulse of width $\tau_{\rm p}$ (here roughly 350 fs) is simply

$$\sigma_{\rm t} = \gamma \frac{\tau_{\rm p}}{\sqrt{n}} \tag{1}$$

where n is the number of detected photons in the measurement interval and γ is a constant of order unity. Here, we demonstrate OTT at this quantum limit by exploiting the precision and agility of a time-programmable frequency comb (TPFC)²⁹ in conjunction with Kalman filter-based signal processing. The improvement over previous LOS-based OTT is large: the minimum received power decreases 10,000-fold from a few nanowatts to a few hundred femtowatts, which means only one out of 100 received frequency comb pulses contains a photon.

We demonstrate this quantum-limited OTT by synchronizing two optical timescales across two different free-space links: a 2-km link with low turbulence in Boulder, CO, USA and a 300 km link with strong turbulence between two mountaintops in Hawaii. Under low turbulence, where the free-space path is indeed reciprocal, the two-way time transfer is nearly quantum-limited; the clocks are synchronized to 246 as/ $\sqrt{P\tau}$ in time deviation and to $4.3 \times 10^{-16}/\sqrt{P\tau^3}$ in fractional frequency (modified Allan deviation), where P is the received power in picowatts and τ is the averaging time in seconds, with respective floors of roughly 35 attoseconds and below 10⁻¹⁸. Over the 300 km horizontal link, the one-way timing signals are still measured at nearly the quantum limit with a power threshold of 270 fW. However, the strong integrated turbulence leads to excess non-reciprocal time-of-flight noise, attributed to multipath effects. Nevertheless, the clocks remain synchronized to 1.6 fs $\tau^{-1/2}$ reaching a floor of 320 attoseconds in time and 2.8 × 10⁻¹⁵ $\tau^{-3/2}$ reaching a floor of 3.1×10^{-19} in frequency. Finally, synchronization is achieved even at attenuated comb powers of 40 μ W with a median received power of 150 fW. This low-power performance is enabled by the robust Kalman filter approach that can tolerate the greater than

National Institute of Standards and Technology (NIST), Boulder, CO, USA, Department of Electrical, Energy and Computer Engineering, University of Colorado, Boulder, CO, USA 3Octosig Consulting, Quebec City, Quebec, Canada. 4Space Dynamics Laboratory, North Logan, UT, USA. 5These authors contributed equally: Emily D. Caldwell, Jean-Daniel Deschenes, Nathan R. Newbury, Laura C. Sinclair. [™]e-mail: nathan.newbury@nist.gov; laura.sinclair@nist.gov

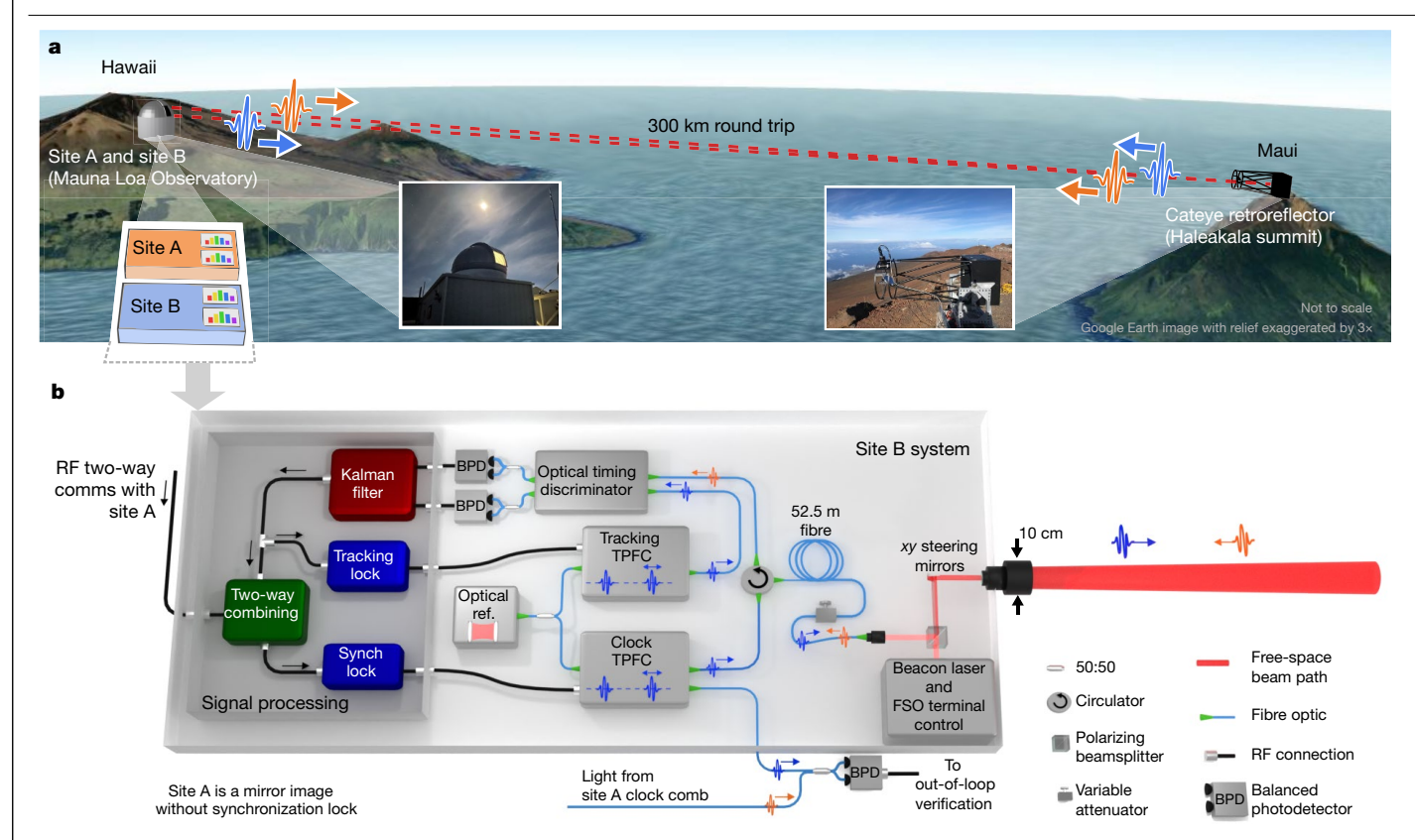


Fig. 1 | **Quantum-limited OTT. a**, The system was tested on a 300 km folded free-space link established between two sites, colocated at the Mauna Loa Observatory (elevation 3,400 m) and a cat-eye retroflector located on the summit of Haleakala (elevation 3,050 m). Colocation of the sites allows a direct, out-of-loop timing verification. **b**, Detailed schematic for site B. (Site A is identical except without the synchronization (Synch) lock.) Each site uses two TPFCs phase locked to a local optical reference. The clock TPFC output defines the local timescale. It is also transmitted across the bidirectional link through a 10-cm aperture free-space optical (FSO) terminal (Extended Data Fig. 1). The

70% signal fades. In comparison to the longest previously reported range for LOS-based OTT²⁴, quantum-limited OTT operates across three times the distance, at 20 times improved update rate using 200 times less comb power and at four times lower aperture diameter, with more than 14 dB greater tolerable link loss. The tolerable link loss of 102 dB exceeds that of future ground-to GEO links with similar 10-cm

Quantum-limited time transfer using a TPFC

apertures and milliwatt comb powers.

The quantum-limited OTT was demonstrated first over a 2 km link at the NIST campus in Boulder and then over the 300 km link between the Hawaiian Islands shown in Fig. 1a. For both, a folded-link geometry enabled direct out-of-loop verification of the synchronization, at the cost of added link loss, but the system could ultimately be used in a point-to-point^{21,24} or multi-node geometry²⁰. For the Hawaii link, operation was mainly limited to overnight and early morning hours because of daytime clouds in the interisland convergence zone

The system is centred around fibre-based, 200-MHz repetition frequency, TPFCs that provide real-time attosecond-level digital control of the pulse timing. A heterodyne timing discriminator²⁹, as shown in Extended Data Fig. 4, measures the time offset between a local tracking TPFC and the incoming clock comb pulse signal with shot-noise limited sensitivity. This time offset acts as an error signal to adjust the digital control of the tracking TPFC to follow the incoming clock

tracking TPFC is used to acquire, track and measure the timing of the incoming clock comb pulse train. Two-way combination of the measured timing signals generates an error signal that is applied at site B for synchronization (text). The filtered comb output powers are 4.0 mW and 5.9 mW for sites A and B (Extended Data Fig. 2), but can be attenuated by the in-line attenuator to mimic links with higher loss. The fibre spools before the FSO terminals compensate for the 300 km of air dispersion. (See also Extended Data Fig. 3 and Methods.) The underlying map in $\bf a$ is from Google Earth with image data from Landsat and Copernicus. RF, radio frequency.

comb pulses (Methods). The commanded tracking-TPFC timing then replicates the timing of the incoming comb pulse train at each site, t_A or t_B , whose difference,

$$\Delta t = \frac{t_{\rm A} - t_{\rm B}}{2} = (\Delta T_{\rm osc} - \Delta T_{\rm cntrl}) + \varepsilon_{\rm NR, turb} + \varepsilon_{\rm qn} + \varepsilon_{\rm combs}$$
 (2)

is a measure of the time offset between the two clock combs, $(\Delta T_{\rm osc} - \Delta T_{\rm cntrl})$, where $\Delta T_{\rm osc}$ is the time offset between the local reference oscillators and $\Delta T_{\rm cntrl}$ is the synchronization feedback to the clock TPFC at site B ($\Delta T_{\rm cntrl} = 0$ for open-loop operation). The fundamental reciprocity of a single spatial mode link 30 means that the time-of-flight, including turbulence effects, should cancel in this two-way comparison of equation (2). Nevertheless, we include a non-reciprocal, turbulence noise term, $\epsilon_{\rm NR,turb}$, for reasons discussed later. The quantum noise term, $\epsilon_{\rm qn^\prime}$ has a standard deviation following equation (1). The system noise, $\epsilon_{\rm combs}$, is typically negligible at short averaging times and low powers, but leads to the flicker floor at long averaging times.

To track the incoming pulses, the incoming clock comb and local tracking comb pulses must overlap in time to within the roughly $2\tau_p$ dynamic range of the timing discriminator. This initial alignment is accomplished by sweeping the tracking comb pulse position in time² and searching for peaks in the heterodyne signal (Fig. 2a). Scintillation from turbulence, however, causes random 100% intensity fluctuations that complicate mapping the peak heterodyne voltage to the incoming pulse location. Using a Kalman filter to aggregate intermittent

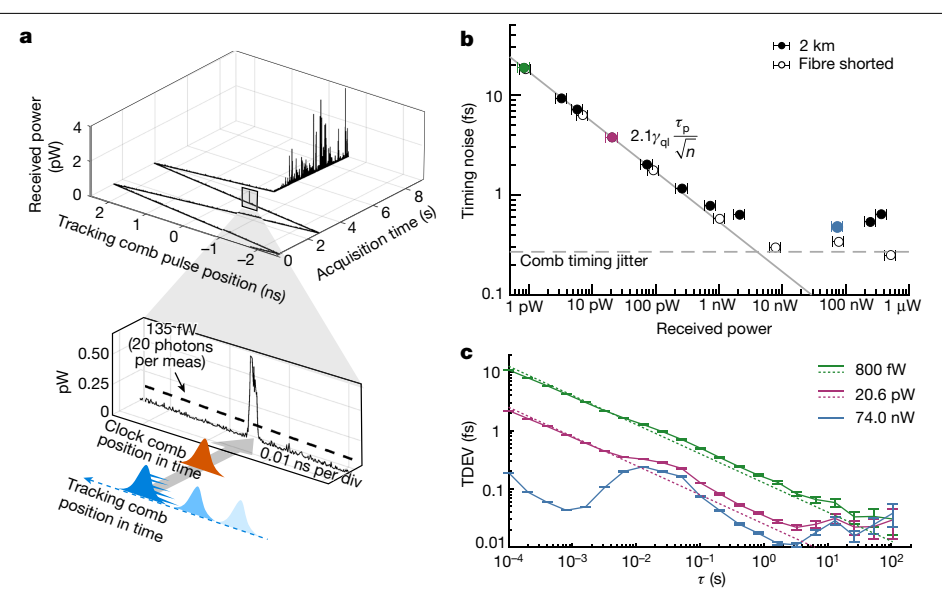


Fig. 2 | Low-power acquisition and quantum-limited performance.

a, Demonstrated signal acquisition over the 300 km Hawaii link. Initially, the local tracking TPFC is swept over its full 5 ns non-ambiguity range in a triangular waveform. At roughly 3 s into the acquisition, a peak in the heterodyne signal indicates a transient temporal overlap between the tracking TPFC and the incoming clock comb (inset). On the basis of the observation of a heterodyne signal above the 135 fW threshold, the signal processor steers the tracking comb back to this location for finer search before initiating the tracking lock at

roughly 5 s into the acquisition. **b**, The timing noise (standard deviation over 600 s) in Δt measured over a shorted link (open circles) and a 2 km free-space link (closed circles). Colours correspond to traces in **c** below. The timing follows the quantum limit from equation (1) for $\gamma = 2.1\gamma_{cl}$ (grey line), where $\gamma_{\rm nl} \approx 0.6$ is the quantum limit for Gaussian pulses (ref. 29 and Extended Data Table 1). c, Time deviations (TDEV) over the 2 km free-space link at received powers of 800 fW and 20.6 pW follow the quantum limit with $y = 2.1y_{cl}$ (dotted lines), until reaching the system noise floor at received powers above 10 nW.

observations of pulse overlap, we can track the estimated temporal position of the incoming pulses, and the associated uncertainty, despite fades. As the estimated position uncertainty decreases, the search space narrows. When the estimated uncertainty reaches 500 fs, the tracking lock is engaged. To detect the weakest possible incoming comb light, the detection bandwidth for the heterodyne timing discriminator should be as narrow as possible given the constraints of atmospheric turbulence phase noise and platform and fibre vibration. We settled on 26 kHz here as a conservative compromise.

For robust operation through signal fades, the timing samples, $t_{\rm A}$ and $t_{\rm B}$, are input into the Kalman filter to generate optimal estimates of the timing with 10–25 Hz effective bandwidth. These Kalman-filtered values are used in equation (2) and input to a 15-Hz bandwidth synchronization lock to steer the site B clock comb. Here, the timing signals used in the two-way combining are communicated from sites A to B by coaxial cable but an optical communications link could be implemented as in ref. 15. The transceiver time delays are calibrated so the pulses from the two clock combs overlap at the out-of-loop verification reference plane located within site B when $\Delta t \rightarrow 0$ (Extended Data Figs. 5 and 6).

At low power and weak turbulence, the two-way time transfer is nearly quantum limited following equation (1) until it reaches the system noise floor (Fig. 2b,c). We apply a roughly 270 fW threshold on the received power for a valid timing measurement, chosen such that the quantum-limited timing noise standard deviation was roughly one-sixth the full timing discriminator dynamic range (Supplementary Information). For comparison, the power threshold for signal acquisition is lower, at roughly 135 fW, selected to limit false detections to fewer than one per day (Methods). These thresholds correspond to n = 40 and 20 photons per signal integration time (19 μ s), respectively, or 0.01 and 0.005 mean photons per comb pulse. The values of n > 1reflect the conservatively chosen threshold to ensure low probability of false detection. Both the acquisition and timing measurements operate at roughly twice the quantum limit because of detector noise power penalty and differential chirp between the tracking comb and incoming comb pulses. There is a negligible contribution from daylight; reflected sunlight would contribute only 10 attowatts within the single-mode heterodyne detection bandwidth.

Demonstration over a 300 km terrestrial free-space link

Figure 3 compares the performance over the 300 and 2 km links in terms of timing synchronization, timing instability and frequency instability. Further data are provided in the Extended Data Figs. 7–10. Although the one-way timing measurements are quantum limited over the strongly turbulent 300 km link, unlike the shorted and 2 km link, their two-way subtraction. Δt , does not reach the quantum limit for reasons discussed below. Nevertheless, it drops below state-of-the-art transportable optical atomic clocks⁹ after only 6 s of averaging time and laboratory optical atomic clocks after 17 s of averaging time²¹.

To demonstrate operation at extreme link loss, the comb power from site B was attenuated to 40 µW leading to a median received power of 150 fW at site A. Despite signal fading 73% time below threshold, timing acquisition and synchronization were still achieved with minimal 2.8 times performance degradation at short times. This attenuation of the site B power is done in the two-way path and is equivalent to operation with 4.0 mW of comb power over a total link loss of 106 dB.

Effects of turbulence on timing

The increased timing noise across the 300 km link is attributed to the strong integrated turbulence and a breakdown in the expected reciprocity in time-of-flight over the single-mode link³⁰. Previous combbased OTT has not seen clear violations in reciprocity even at 100 km (refs. 14-24). However, the enhanced sensitivity of quantum-limited OTT means we can probe timing fluctuations at the attosecond-level during deep signal fades when the effects of multipath interference are at their strongest.

This excess noise is illustrated best in the power spectral densities (PSDs) of Δt and its counterpart $\bar{t} = (t_A + t_B)/2$ (Fig. 4). The latter measures the time-of-flight and shows the expected piston noise

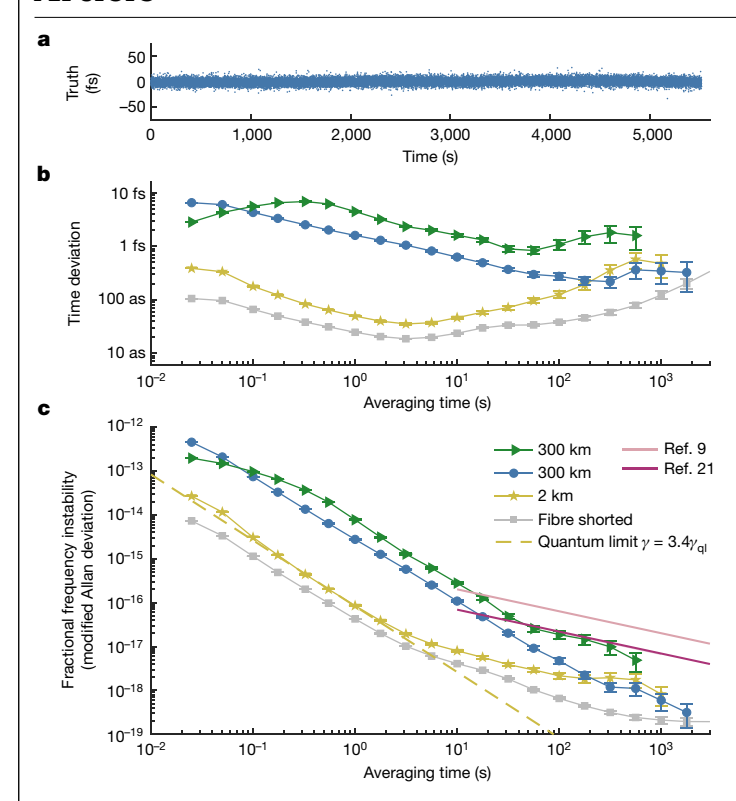


Fig. 3 | OTT measured by out-of-loop timing comparison. a, Clock time difference (out-of-loop verification) across the 300 km link for 4.0 mW comb power and 14 pW median received power. **b**,**c**, Time deviation (**b**) and fractional frequency instability (c) (modified Allan deviation) across the 300 km link at 4.0 mW comb power with 14 pW median received power (blue circles) and 40 μW attenuated comb power with 150 fW median received power (green triangles). Also shown are data from the 2 km link at 30 pW received power (yellow stars) and shorted (grey dots). At low turbulence over the 2 km link, the performance is nearly quantum limited (yellow dashed line for $\gamma = 3.4\gamma_{ol}$). Over 300 km, performance is limited by non-reciprocal multipath atmospheric turbulence at short times. The time deviations follow 1.6 fs/ $\sqrt{\tau}$ and 49 as/ $\sqrt{\tau}$ for the 300 km and 2 km links, plateauing at 475 as. The corresponding modified Allan deviations follow $2.8 \times 10^{-15} \tau^{-3/2}$ and $8.5 \times 10^{-17} \tau^{-3/2}$, reaching a floor of 3.1×10^{-19} . For context, instability curves are provided for comparisons of physically separated clocks involving transportable (light pink) and laboratory optical clocks21 (dark pink).

(time-of-flight pulse wander) with its $f^{-8/3}$ Kolmogorov scaling 31,32 . A fit to this piston noise, assuming a $10 \, \mathrm{m \, s^{-1}}$ wind speed on the basis of typical meteorological data, generates an estimate of the integrated turbulence strength, LC_n^2 where C_n^2 is the turbulence structure function and L is the link distance. The values of LC_n^2 range over two orders of magnitude, from 1×10^{-11} to $1 \times 10^{-9} \, \mathrm{m^{1/3}}$, for measurements overnight and into the early morning hours (Fig. 4 inset). Note that the use of a folded-link geometry only increases, rather than cancels, the piston-induced time-of-flight noise.

The PSD of \bar{t} shows excess time-of-flight noise (shaded region), beyond the piston noise, out to the Greenwood frequency of roughly 300 Hz before dropping to the quantum-limited white noise floor. The PSD of Δt (open loop) follows the expected f^{-3} phase noise of the reference oscillators but shows similar excess timing noise (shaded purple region), although suppressed by roughly 7–11 dB from \bar{t} . This excess noise on Δt limits the out-of-loop synchronization, yielding the white noise floor shown in Fig. 4 and the corresponding elevated instabilities in Fig. 3. We attribute it to multipath interference due to strong atmospheric turbulence across the 300 km horizontal link. As the turbulence strength increases, the pulse shape itself can distort and spread after transmission 31,33,34 . We speculate these multipath related distortions

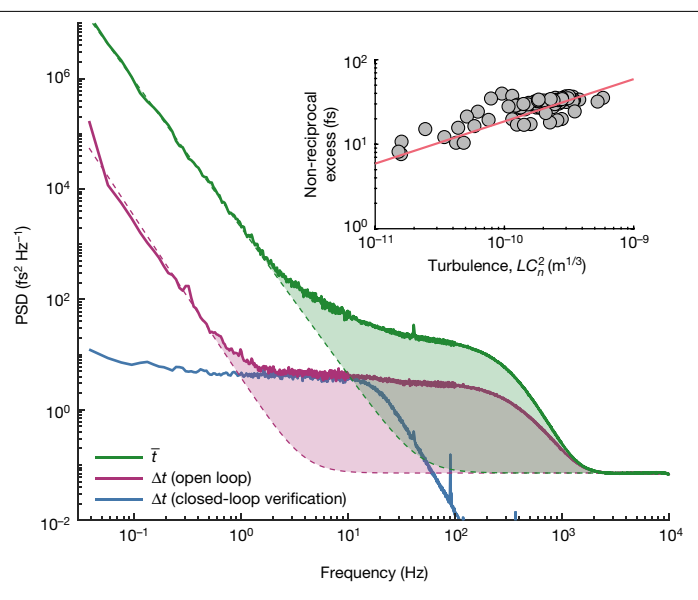


Fig. 4 | PSDs measured over the strong turbulence of the 300 km link. Timing PSD for a representative 90 min measurement for $\Delta t = (t_{\rm A} - t_{\rm B})/2$ (purple solid line), the time-of-flight term given by $\bar t = (t_{\rm A} + t_{\rm B})/2$ (green solid line) and out-of-loop synchronization verification (blue solid line). Shaded regions indicate excess noise beyond the expected reference oscillator noise and piston noise values, for Δt and $\bar t$, respectively, as well as the shared quantum noise floor (dashed lines). The excess timing noise on Δt sets the floor for the out-of-loop timing below the 15 Hz synchronization bandwidth. Inset shows the non-reciprocal excess versus LC_n^2 for 10 min intervals over many runs (grey circles). The solid red line illustrates the linear trend with integrated turbulence strength.

will depend on the pulse chirp, which differs between clock combs leading to the limited 7–11 dB suppression in the reciprocal measurement. Whereas such strong turbulence effects are challenging to analyse theoretically, the noise should increase with integrated turbulence, which is indeed the case as illustrated in the inset of Fig. 4.

Future long-distance ground-to-space links

Figure 5 puts the performance and size, weight, power and cost (SWaP-C) of quantum-limited OTT in context with previous work and future space-based OTT. The current 10 cm apertures and 4.0 mW comb powers bode well for future low-SWaP-C space instruments³⁵. Moreover, the use of 10 cm apertures for the ground as well as satellite terminals permits compact ground stations. For applications such as global time distribution, clock-based geodesy or very long baseline interferometry, the satellite would include OTT terminals and a high-performance oscillator^{36–38}. Relativistic tests or dark-matter searches would require an atomic optical clock onboard the satellite, along with the OTT terminals.

Whereas GEO-to-ground links are 100 times farther than the Hawaii link, the path integrated turbulence is roughly 100 times lower. As a result, for paired 10-cm aperture telescopes, the total link loss is similar to that shown in Fig. 5 (Supplementary Information) and the conservative 102 dB tolerable loss exceeds the estimated ground-to-GEO link loss by 11 dB. A fourfold increase in the ground aperture should increase the reach to *cis*-lunar orbits. Because the integrated turbulence is about 100 times lower than for the Hawaii link, ground-to-space OTT should not suffer from the same level of non-reciprocal timing noise from multipath effects. However, the turbulence-induced piston noise will no longer perfectly cancel as the up- and down-going comb pulses traverse the turbulent atmosphere with a 0.12-s time offset, roughly the time-of-flight to GEO. As a result, there is a differential piston noise

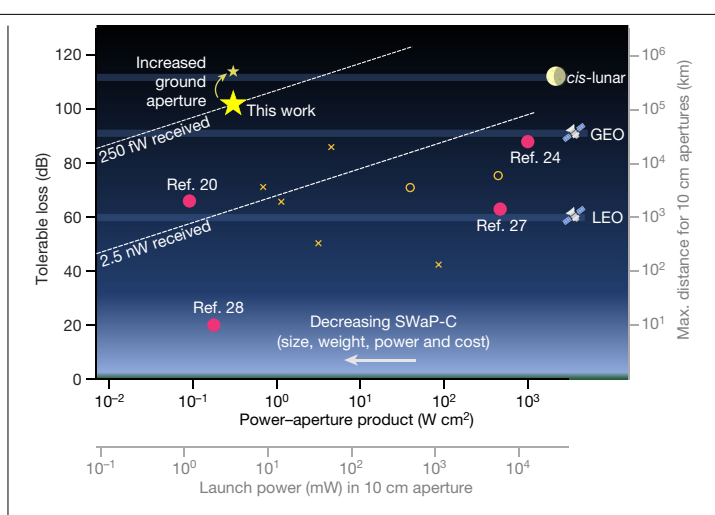


Fig. 5 | Ground-to-space time transfer. Future free-space OTT will require operation at long distance, set by tolerable link loss, and low SWaP-C, largely set by the power-aperture product. The current demonstration (large yellow star) achieves the highest tolerable loss of 102 dB at the very low poweraperture product of 0.3 W cm² as compared to previous comb-based timefrequency transfer or OFT (magenta circles)^{20,24,27,28}. The linear trade-off (white dashed lines) between tolerable loss or maximum (Max.) distance and poweraperture product is set by the received power threshold, as shown for the LOS comb-based OTT (2.5 nW) and quantum-limited OTT (250 fW) with both curves assuming a 10 cm aperture. For an additional comparison, several optical communication missions are shown (orange circles for GEO and orange crosses for LEO) $^{\rm 44-49}.$ The lower bottom and far right axes assume matched 10 cm apertures, 2 dB channel loss, 6 dB total transceiver loss and 6 dB additional coupling loss (Supplementary Information). The maximum projected distance for the current OTT exceeds the 35,786 km GEO altitude and even reaches the 10 times farther cis-lunar distances if the ground aperture is increased to 40 cm, while leaving the space-based aperture at 10 cm (small yellow star).

contribution that limits the time deviation to ≈ 2 fs/ $\sqrt{\tau}$ and modified Allan deviation to $\approx 4 \times 10^{-15} \tau^{-3/2}$ (Supplementary Information). Purely coincidentally, these values are close to the data of Fig. 3 although of very different origin. Nevertheless, the residual instability is below state-of-the-art optical clocks for $\tau > 10$ s of seconds. OTT could then compare two optical clocks in different locations without degradation by means of common view, or a ground clock to a space-based clock for tests of relativity 1-3. Active clock synchronization would be limited to a bandwidth of roughly $1/(8 \times 0.12 \text{ s}) = 1$ Hz, or roughly ten times lower than the Hawaii link. Therefore, applications that require high coherence between ground and space might combine active synchronization (for observation times beyond 2 s) with near-real-time post-processing of the time samples (for observation times below 2 s).

Although the link margin is more than sufficient for OTT to low to mid-Earth orbits (LEO/MEO), these involve up to 8 km s⁻¹ velocities with significant resulting Doppler shifts, other relativistic effects and point-ahead. Relativistic effects are in principle calculable and non-reciprocity from point-ahead have been shown to be negligible after correction³⁹⁻⁴¹. However, the strong Doppler shifts will significantly complicate signal acquisition and signal processing, while potentially introducing systematics. For example, signal acquisition within the 26-kHz detection bandwidth requires orbit velocity knowledge to ±2 cm s⁻¹. In addition, coupling of Doppler shifts to optical dispersion can mimic time shifts, causing systematic errors. For these reasons, quantum-limited OTT to LEO/MEO orbits will require an even more advanced system. It is likely such a system will require a hybrid approach that combines comb-based OTT with continuous wave laser-based OFT to assist with the frequency acquisition and tracking of the large Doppler shifted signals.

Figure 5 includes several optical communication missions. Ouantum-limited OTT might piggyback on future coherent optical communication links, which would be facilitated by its low power threshold of -96 dBm either by use of a shared aperture or separately steered subaperture. It also includes several demonstrations of OFT by means of two-way transmission of a continuous wave laser, which reaches extremely low instabilities over low turbulence, kilometre-scale links^{26–28}. The tolerable loss (and therefore distance) for OFT could be significantly extended by operation near the shot-noise limit depending on the tolerance for cycle slips⁴². However, signal interruptions from turbulence, weather, platform motion and/or multiplexed operation to different sites will result in penalties in the frequency transfer⁴³ and, critically, prevent measurement of the relative time offset between clocks, the quantity of interest for many applications. Quantum-limited OTT, on the other hand, can track the relative time with femtosecond precision even if the link availability is limited to seconds interspersed across hours, days or longer.

Conclusion

By operating near the quantum limit, this OTT requires 10,000 times less power than previous LOS approaches. Here, we show attosecond time transfer over record distances of 300 km and record link losses of 102 dB, while transmitting only the 4.0 mW output from a compact, unamplified frequency comb. At low turbulence strengths, the time deviation is as low as 35 attoseconds at 3 s averaging. Under strong turbulence, the time deviation drops as low as 220 attoseconds at roughly 300 s of averaging: well below what is needed for distributed coherent sensing, redefinition of the second and tests of fundamental physics $^{1-12}$.

The combination of this level of performance, low-power aperture product and the ability to operate at 102 dB link loss without adaptive optics will enable future low SWaP-C OTT from geosynchronous orbits (GEO) to portable ground-based clocks for time transfer, geodesy, relativity tests or distributed sensing. Indeed, with a four times increase in ground terminal aperture, future OTT could even reach *cis*-lunar orbits.

Online content

Any methods, additional references, Nature Portfolio reporting summaries, source data, extended data, supplementary information, acknowledgements, peer review information; details of author contributions and competing interests; and statements of data and code availability are available at https://doi.org/10.1038/s41586-023-06032-5.

- Derevianko, A. et al. Fundamental physics with a state-of-the-art optical clock in space. Quantum Sci. Technol. 7, 044002 (2022).
- Mehlstäubler, T. E., Grosche, G., Lisdat, C., Schmidt, P. O. & Denker, H. Atomic clocks for geodesy. Rep. Prog. Phys. 81, 064401 (2018).
- Altschul, B. et al. Quantum tests of the Einstein equivalence principle with the STE-QUEST space mission. Adv. Space Res. 55, 501–524 (2015).
- Derevianko, A. & Pospelov, M. Hunting for topological dark matter with atomic clocks. Nat. Phys. 10, 933–936 (2014).
- Kolkowitz, S. et al. Gravitational wave detection with optical lattice atomic clocks. Phys. Rev. D 94, 124043 (2016).
- The Event Horizon Telescope Collaboration. First M87 event horizon telescope results. II. Array and instrumentation. Astrophys. J. Lett. 875, L2 (2019).
- Kurczynski, P. et al. The Event Horizon Explorer mission concept. In Proc. Space Telescopes and Instrumentation 2022: Optical, Infrared, and Millimeter Wave (eds Coyle, L. E. et al.) Vol. 12180. 215–224 (SPIE. 2022).
- Warren, Z. & Fields, R. Optical crosslinks and satellite synchronization for GNSS, communications, and beyond. GPS Solut. 26, 64 (2022).
- Takamoto, M. et al. Test of general relativity by a pair of transportable optical lattice clocks. Nat. Photonics https://doi.org/10.1038/s41566-020-0619-8 (2020).
- Lisdat, C. et al. A clock network for geodesy and fundamental science. Nat. Commun. 7, 12443 (2016).
- Riehle, F. Towards a redefinition of the second based on optical atomic clocks. C.R. Phys. 16, 506–515 (2015).
- 2. Bize, S. The unit of time: present and future directions. C.R. Phys. 20, 153–168 (2019).
- Itano, W. M. et al. Quantum projection noise: population fluctuations in two-level systems. Phys. Rev. A 47, 3554–3570 (1993).

32.

- Giorgetta, F. R. et al. Optical two-way time and frequency transfer over free space. Nat. Photonics 7, 434-438 (2013).
- Deschênes, J.-D. et al. Synchronization of distant optical clocks at the femtosecond level. 15 Phys. Rev. X 6, 021016 (2016).
- Bergeron, H. et al. Tight real-time synchronization of a microwave clock to an optical 16. clock across a turbulent air path. Optica 3, 441 (2016).
- Sinclair, L. C. et al. Synchronization of clocks through 12km of strongly turbulent air over a city. Appl. Phys. Lett. 109, 151104 (2016).
- 18. Sinclair, L. C. et al. Comparing optical oscillators across the air to milliradians in phase and 10-17 in frequency. Phys. Rev. Lett. 120, 050801 (2018).
- Bergeron, H. et al. Femtosecond time synchronization of optical clocks off of a flying quadcopter. Nat. Commun. 10, 1819 (2019).
- 20. Bodine, M. I. et al. Optical time-frequency transfer across a free-space, three-node network. APL Photonics 5, 076113 (2020).
- Boulder Atomic Clock Optical Network (BACON) Collaboration. et al. Frequency ratio 21 measurements at 18-digit accuracy using an optical clock network, Nature 591, 564-569 (2021).
- 22. Ellis, J. L. et al. Scaling up frequency-comb-based optical time transfer to long terrestrial distances, Phys. Rev. Appl. 15, 034002 (2021).
- Shen, Q. et al. Experimental simulation of time and frequency transfer via an optical satellite-ground link at 10-18 instability. Optica 8, 471-476 (2021).
- 24. Shen, Q. et al. Free-space dissemination of time and frequency with 10-19 instability over 113 km. Nature 610, 661-666 (2022).
- Fujieda, M. et al. Carrier-phase two-way satellite frequency transfer over a very long baseline. Metrologia 51, 253 (2014).
- 26. Djerroud, K. et al. Coherent optical link through the turbulent atmosphere. Opt. Lett. 35, 1479-1481 (2010)
- Kang, H. J. et al. Free-space transfer of comb-rooted optical frequencies over an 18 km open-air link. Nat. Commun. 10, 4438 (2019).
- Gozzard, D. R. et al. Ultrastable free-space laser links for a global network of optical atomic clocks. Phys. Rev. Lett. 128, 020801 (2022).
- Caldwell, E. D., Sinclair, L. C., Newbury, N. R. & Deschenes, J.-D. The time-programmable frequency comb and its use in quantum-limited ranging. Nature 610, 667-673 (2022).
- 30. Shapiro, J. H. Reciprocity of the turbulent atmosphere. J. Opt. Soc. Am. 61, 492-495
- 31. Andrews, L. C. & Phillips, R. L. Laser Beam Propagation through Random Media (SPIE,
- optical time-frequency transfer. Phys. Rev. A 89, 023805 (2014). Liu, C. H. & Yeh, K. C. Pulse spreading and wandering in random media. Radio Sci. 14, 33

Sinclair, L. C. et al. Optical phase noise from atmospheric fluctuations and its impact on

- 925-931 (1979).
- Young, C. Y. in Free-Space Laser Communication and Laser Imaging II Vol. 4821 (eds. 34. Ricklin, J. & Voelz, D. G.) 74-81 (SPIE, 2002).
- Stahl, H. P., Stephens, K. R., Henrichs, T., Smart, C. & Prince, F. A. Single-variable parametric 35 cost models for space telescopes. OE 49, 073006 (2010)

- Abich, K. et al. In-orbit performance of the GRACE follow-on laser ranging interferometer. Phys. Rev. Lett. 123, 031101 (2019)
- 37. Świerad, D. et al. Ultra-stable clock laser system development towards space applications. Sci. Rep. 6, 33973 (2016).
- Numata, K. et al. Progress and plans for a U.S. laser system for the LISA mission. In Proc. International Conference on Space Optics—ICSO 2018(eds Cugny, B. et al.) Vol. 11180, 152-159 (SPIE, 2019).
- Swann, W. C. et al. Measurement of the impact of turbulence anisoplanatism on precision free-space optical time transfer. Phys. Rev. A 99, 023855 (2019).
- Robert, C., Conan, J.-M. & Wolf, P. Impact of turbulence on high-precision ground-satellite frequency transfer with two-way coherent optical links. Phys. Rev. A 93, 033860 (2016).
- Stuhl, B. K. Atmospheric refraction corrections in ground-to-satellite optical time transfer. Opt. Express 29, 13706 (2021).
- Francis, S. P. et al. Weak-light phase tracking with a low cycle slip rate. Opt. Lett., OL 39, 5251-5254 (2014).
- Tønnes, M. B. K. et al. Coherent fiber links operated for years: effect of missing data. 43. Metrologia 59, 065004 (2022).
- Kuwahara, T. et al. Laser data downlink system of micro-satellite RISESAT, In Proc. Small 44. Satellite Conference https://digitalcommons.usu.edu/smallsat/2013/all2013/57 (2013).
- Kolev, D. et al. Status update on laser communication activities in NICT. In Proc. 2022 IEEE 45. International Conference on Space Optical Systems and Applications (ICSOS) 36-39 (IEEE, 2022).
- Carrasco-Casado, A. & Mata-Calvo, R. in Springer Handbook of Optical Networks (eds. Mukherjee, B. et al.) 1057-1103 (Springer, 2020).
- Robinson, B. S. et al. TeraByte InfraRed Delivery (TBIRD): a demonstration of large-volume direct-to-Earth data transfer from low-Earth orbit. In Proc. Free-Space Laser Communication and Atmospheric Propagation XXX (eds Boroson, D. M. & Hemmati, H.) Vol. 10524, 253-258 (SPIE, 2018).
- Wright, M. W., Kovalik, J., Morris, J., Abrahamson, M. & Biswas, A. LEO-to-ground optical communications link using adaptive optics correction on the OPALS downlink. In Proc. Free-Space Laser Communication and Atmospheric Propagation XXVIII (eds Boroson, D. M. & Hemmati, H.) Vol. 9739, 973904 (International Society for Optics and Photonics, 2016).
- Gregory, M. et al. Commercial optical inter-satellite communication at high data rates. Opt. Eng. 51, 031202 (2012).

Publisher's note Springer Nature remains neutral with regard to jurisdictional claims in published maps and institutional affiliations.

Springer Nature or its licensor (e.g. a society or other partner) holds exclusive rights to this article under a publishing agreement with the author(s) or other rightsholder(s): author self-archiving of the accepted manuscript version of this article is solely governed by the terms of such publishing agreement and applicable law.

© This is a U.S. Government work and not under copyright protection in the US; foreign copyright protection may apply 2023

Methods

Overview of OTT operation

The steps necessary for operation of the time transfer system are as follows (Extended Data Fig. 3):

- (1) Initial calibration (done once after transceiver construction):
 - (a) Calibrate the transceiver time delay between the tracking comb reference plane (used to measure the time offset between the local tracking and clock combs at the tracking comb initialization step below) and the clock comb reference plane (used as out-of-loop verification plane). This calibrated time delay depends only on fibre path lengths in the transceiver, which are minimized and temperature controlled to reduce drift (Extended Data Fig. 5).
 - (b) Calibrate the timing discriminator for both optical timing error and incoming optical power (Extended Data Fig. 4).
 - (c) Calibrate the out-of-loop verification channel voltage-to-time scaling.
- (2) Pre-operation steps (done before every time transfer measurement):
 - (a) Lock the clock comb and tracking comb to the local reference oscillator (portable cavity-stabilized laser in this experiment).
 - (b) Initialize the tracking comb time offset by adjusting its zero-time offset to coincide with its pulse overlapping the local clock comb at the tracking comb reference plane.
 - (c) Generate an initial estimate of the carrier frequency offset between the local tracking comb and incoming clock comb. Here, this estimate is based on measured cavity-stabilized laser frequencies and comb locking parameters.
- (3) Optical link acquisition. Establish bidirectional coupling of the transmitted clock comb light into single-mode optical fibre after propagation across the free-space link (Extended Data Fig. 1).
- (4) Tracking comb timing acquisition. Search for timing overlap between the incoming clock comb and local tracking comb at each site (Fig. 2a and later discussion in Methods).
- (5) Tracking comb lock. Actively feedback to the local tracking comb timing to maintain overlap with the incoming clock comb pulses to within the dynamic range of the optical timing discriminator (Extended Data Fig. 4). In addition, actively feedback to the tracking comb frequency to keep the heterodyne signal between the tracking and local clock combs centred within the 26 kHz detection bandwidth.
- (6) Note that the Kalman filter continuously tracks of the timing uncertainty between the local tracking and incoming clock comb. In the event of a signal fade from turbulence, if this uncertainty is too large, the tracking comb timing is re-acquired as discussed below and in the main text.
- (7) Communication between sites (site A to B). Site A continuously transmits back the received timing to site B so that the clock timing offset can be calculated by means of the two-way timing calculation.
- (8) Synchronization (site B). The clock timing offset is input to the synchronization loop to adjust the clock comb at site B. At the initiation of the synchronization loop, the tracking comb timing at site A is adjusted to avoid loss of tracking (Methods).
- (9) Out-of-loop verification. Once synchronization has been activated, measure the timing overlap of the two clock combs at the out-of-loop verification channel (Extended Data Fig. 6).

Timing discriminator operation

As shown in Extended Data Fig. 5, the optical timing discriminator uses the birefringence of polarization-maintaining (PM) optical fibre to generate two interferograms in which the lead and lag positions of the incoming clock comb pulse and local tracking comb pulses are switched. The signals that are output from each balanced detector sit at a heterodyne frequency set by the offset between the two comb's carrier frequencies. Because we demodulate the signals, this frequency offset must be known a priori to $\pm 13~\rm kHz$ during acquisition, but after acquisition the frequency offset is tracked and adjusted to centre the

demodulation frequency. Initial knowledge of the carrier frequency offset to within ± 13 kHz (fractional frequency knowledge of 6.8×10^{-11} at the optical carrier frequency) can be provided by (1) measuring the reference oscillator frequencies against a GPS disciplined oscillator, (2) use of a coarser frequency transfer over a comms link as has been done previously or (3) past estimates from a Kalman filter. Alternatively, the acquisition could include a search over frequency, but this additional search has not been implemented here. The demodulation frequency is set to differ between sites, nominally at values of 10 and 12 MHz to avoid cross talk from internal reflections within the free-space optical terminals.

The output of the timing discriminator is then the magnitude of the two demodulated signals, $|V_I|$ and $|V_2|$. After calibration, the sum of their squares provides a measure of the incoming clock comb power, in watts, and their normalized relative values provides a measure of the relative timing of the incoming clock comb pulse train with respect to the local tracking comb, in femtoseconds.

Timing discriminator signal power calibration

As with previous comb-based OTT using LOS, the input power is measured by calibrating the heterodyne signal amplitude 15,24 but in this case the signals from the timing discriminator are used. (Direct detection of the incoming power at the 100 fW level would otherwise be challenging). For this heterodyne detection, the power is given by $P = C_p[(|V_1|^2 + |V_2|^2)/2]$, where the calibration factor, C_p has units of W V-2 and is a function of the local tracking comb power on the detector, pulse shape and dispersion, and timing imbalance of the optical timing discriminator. To measure this calibration constant, the link is shorted, attenuated to low powers and synchronized. We then measure the value of $(|V_1|^2 + |V_2|^2)/2$. Next, we measure the total clock comb optical power at the input of the four balanced detector input ports using a calibrated power meter. On the basis of repeated calibrations, we expect this calibration constant to be accurate to within $\pm 20\%$.

This power calibration applies to the normal operation in which the demodulated signals are around half their peak values (Extended Data Fig. 5). During acquisition, the two demodulated squared signals are added together with a temporal delay that reflects the linearly scanned tracking comb. As a result, the peak demodulated voltages are roughly twice higher for the same optical power, and the calibration factor is ideally four times lower. In reality, for the delays here, the increase is closer to a factor of two as the operation point is not fully half of the peak voltage giving $C_{\rm p,acg} \approx C_{\rm p}/2$.

Timing discriminator timing error calibration

The timing error is calculated on the basis of the normalized difference of the two demodulated voltages by $\delta t = f_{td}(E)$, where $E = (|V_1| - |V_2|)/(|V_1| + |V_2|)$ and $f_{rd}(E)$ is the calibration function. $f_{rd}(E)$ is determined in a separate shorted calibration by deliberately offsetting the clock and tracking comb pulse and then measuring the corresponding error signal, as shown in Extended Data Fig. 4. Because the error signal is normalized by the sum of the two demodulated signals, the timing error is insensitive to common-mode (for example, turbulence-induced) amplitude fluctuations between the channels. Furthermore, the performance of the overall system is insensitive to small changes in the calibration function, for example because of changes in the differential pulse dispersion, as the feedback seeks to lock this error signal δt to zero (Extended Data Fig. 4). Moreover, the fact that the timing discriminator's differential delay arises from the difference in propagation constant of the two fibre polarization modes means that the temperature stability requirements are loose.

Quantum-limited operation

Both quantum-limited acquisition and quantum-limited operation depend on the signal-to-noise ratio of the timing discriminator. If that signal-to-noise ratio is shot-noise limited, then the timing discriminator

is operating at the standard quantum limit. We consider that limit under the assumption of heterodyne detection.

We first consider acquisition. Acquisition uses the average mean-squared voltage detected by the timing discriminator, $(|V_1|^2 + |V_2|^2)/2$ to search for pulse overlap. The detector noise level is 1.7 dB above shot noise set by the local tracking comb. On the basis of this noise level, we very conservatively set a threshold value of roughly $(98 \, \mu V)^2$, which yields a false trigger rate of less than once per day. Given $C_{\rm p,acq}$, this threshold corresponds to $P_{\rm thresh,acq} \approx 135$ fW, or roughly 20 photons for the sample time of $(2 \times 26 \, {\rm kHz})^{-1} = 19 \, \mu {\rm s}$ (or 0.005 mean photons per comb pulse) corresponding to the 26 kHz heterodyne detection bandwidth.

Next, we consider quantum-limited operation of the timing discriminator in its estimate of the timing error, δt , between the clock comb and tracking comb pulses, for example, the value of γ in equation (1). To find the quantum limit, we consider heterodyne detection between two unchirped, Gaussian pulses offset in time. (The Gaussian shape avoids sidelobes that can lead to false timing error values and also corresponds to the Gaussian filters used in our apparatus). This simple configuration is equivalent to considering the output from only one arm of the timing discriminator. For timing measurements, we define $\delta t = 0$ to correspond to a pulse separation equal to the full-width at half-maximum, τ_p , of the pulse intensity. As discussed in ref. 29, this yields a timing error of equation (3) with $\gamma_{q1,1} = (2\ln(2)\sqrt{\eta})^{-1}$, where η is the detector quantum efficiency. For the two-way time transfer, assuming an equal number of received photons at each site, there is an additional factor of $\sqrt{2}$, giving

$$\gamma_{\rm ql} = \frac{1}{2\sqrt{2} \ln(2)\sqrt{\eta}} \approx 0.6 \tag{3}$$

In the actual system, we use the dual outputs of the unbalanced Mach–Zehnder interferometer. In that case, n is the total number of received photons. Furthermore, there is a roughly 1.7 dB penalty, D, owing to detector noise, as discussed above. Finally, in our system, the largest penalty results from differential dispersion between the incoming clock comb pulses and the local tracking comb pulse. To lowest order, this causes broadening of the temporal signal by a factor C and a corresponding reduction in peak height by C, leading to a C^2 increase in γ . The differential dispersion contains higher orders that lead to distortions of the pulse shape beyond broadening, but this first-order model is sufficient to characterize the degradation in the factor γ , as

$$\gamma = (DC^2)\gamma_{\rm ql} \tag{4}$$

Experimental values for γ , C and other relevant parameters are given in Extended Data Table 1. We set a power threshold for a 'valid' timing discriminator measurement of 264 fW at site A and 283 fW at site B (Extended Data Fig. 2). These are chosen conservatively to remain in the linear regime of the timing discriminator curve (Extended Data Fig. 4) despite the additive shot noise in the detected signal (and including the 1.7 dB detector noise penalty). At this threshold, additive noise leads to a noise level in E of ± 0.3 (two sigma), which covers $\pm 40\%$ of the shaded region in Extended Data Fig. 4. This power level corresponds to roughly 40 photons in a sample time of ± 0.2 0 kHz)⁻¹ = 19 ± 0.2 1 mean photons per comb pulse).

Free-space optical terminals

The terminals are low loss, fibre coupled, single-transversal-mode and fully reciprocal for the frequency comb light following the design of ref. 50. For the pair of terminals used here (Extended Data Fig. 1), the total 'fibre-to-fibre' loss for comb light between them over a short distance is measured to be 3.3 dB, which includes roughly 2 dB of loss from the optical components and an additional roughly 1.3 dB of coupling loss into the single-mode fibre.

Unlike ref. 50, we use a larger 10 cm beam expander and use a focal plane array (FPA) for detection of the beacon laser for the much longer span of 300 km. The 10 cm aperture was chosen on the basis of commercially available optics and to be larger than the maximum expected Fried parameter. The received beacon is directed to the FPA of an InGaAs camera (Extended Data Fig. 1). For operation at low received powers, the beacon is synchronously modulated and detected at half the camera frame rate, allowing for real-time background subtraction. The beam position on the FPA is maintained at a precalibrated location through feedback to the galvo mirror. Additionally, the beacon power integrated over the region of interest and recorded.

The use of galvo mirrors as in ref. 50 and the FPA provides means of a broad search for the beacon enabling link acquisition after coarse initial pointing. A visible camera with telescopic lens provides the gross initial pointing, aided by an 830 nm, broad angle beacon transmitted through the cat-eye reflector and a matched 830 nm bandpass filter in front of the camera.

Dispersion balancing over the 300 km link

As dispersion amounts to a decrease in both the detection sensitivity and the timing sensitivity, we must compensate for the additional group delay dispersion of the 300 km of air (and also to maintain the accuracy of the power and timing slope calibrations). Using 70,000 pascal for air pressure, 10 °C for air temperature, 25% relative humidity and 450 ppm for CO₂ mole fraction, we estimate the group velocity dispersion of the air in Hawaii to be $\beta_2=7.43\times 10^{-30}~\text{s}^2\text{m}^{-1}$. In comparison, at 1,560 nm, PM1550 fibre has dispersion of $\beta_2=-2.18\times 10^{-26}~\text{s}^2\text{m}^{-1}$. Therefore, we can compensate for the 297 km of air by adding 101 m of PM1550 fibre to the fibre path length already in place for a shorted measurement. As a final fine-tuning step, we measure the pulse widths across the atmosphere and minimize the width of the interference signal. This optimization yields a total PM1550 fibre length of 105 m.

Tracking comb timing acquisition and lock

At the onset of operation or after a long fade, the system must acquire the tracking lock between the local tracking comb and the incoming clock comb. This acquisition is accomplished with a Kalman filter-based search. As discussed in the main text, this search is based on the timing discriminator signal power output value of $(|V_1(t)|^2 + |V_2(t - r\tau_p)|^2)/2$, where r is the scanning rate of the tracking comb. This signal is proportional to the input clock comb pulse power. A voltage threshold is applied that corresponds to roughly 135 fW at zero pulse time offset (Timing discriminator operation).

The search for temporal overlap is complicated by turbulence and by differential clock drift between the unsynchronized sites. Intensity scintillation from turbulence causes the signal intensity to fluctuate randomly, complicating the mapping between peak heterodyne signals and the location of the incoming clock comb pulses in time. Additionally, differential drift between the two cavity-stabilized lasers will cause the incoming clock comb pulses to move in time relative to the local comb pulses on the timescale of the search. To overcome these challenging conditions, we tightly couple the acquisition algorithm with a Kalman filter that keeps track of the estimated position of the incoming clock comb time and most critically, its associated uncertainty.

Starting from a completely unknown received comb timing with respect to the tracking comb, the search controller sweeps the tracking comb through the full 5 ns non-ambiguity range until a signal is observed above threshold, indicating a momentary coincidence between the tracking comb and the received clock comb. This signal is then used to update the Kalman filter's state and uncertainty estimates.

The effect of the Kalman filter (KF) is to aggregate these intermittent observations of the temporal overlap into a consistent picture for the estimated trajectories of $t_a^{\rm KF}$ and $\sigma_{{\rm KF},ta}^2$ (for the measurement of the received clock comb pulse time from site B at site A). These are in turn

used by the search controller to decide the search pattern swept by the tracking comb. Specifically, the tracking comb timing is swept as a triangle waveform through a search space set by $t_{\rm a}^{\rm KF}\pm 3\sigma_{\rm KF,ta}$. Each individual observation of the interference signal improves the accuracy of $t_{\rm a}^{\rm KF}$ and reduces its estimated uncertainty $\sigma_{\rm KF,ta}^2$, narrowing the size of the search span and rapidly converging on the true position of the received comb pulses. Finally, once the position uncertainty is small enough $(\sigma_{\rm KF,ta}\!<\!2\tau_{\rm p})$, the tracking comb control switches to tracking $t_{\rm a}$ continuously.

In practice, given the good performance of the cavity-stabilized continuous wave reference lasers and the high timing accuracy of each detection of temporal overlap between the tracking and incoming clock comb pulses, the first observation event collapses the uncertainty of the prediction from 5 ns to roughly 1 ps. This leaves almost exclusively a contribution from the unknown initial frequency offset between the sites, which produces a ramp in time offset. As soon as a second observation is produced, the frequency offset is determined and the uncertainty becomes very small, dominated by the random link delay fluctuations. Depending on the received link fades, acquisition either completes almost immediately after these initial observations, or the tracking comb sweeps over a small range centred on the predicted location until the received power crosses threshold again.

However, at the lower received powers, there is a significant probability that the signal is not observable (below threshold) at the moment in the sweep that the tracking comb and incoming clock comb pulses overlap temporally. This lack of signal does not have a direct effect on the Kalman filter's estimates, but it does have an indirect one: the uncertainty in the clock time offset grows over time in the absence of observations due to the inherent statistics of the reference oscillator noises. Thus, if too much time passes between observations, the search space will naturally increase, up to the maximum of the full 5 ns search space, essentially resetting the search process.

Similarly, when the system is in tracking mode but experiences a fade, the Kalman filter's uncertainty can be used to decide whether a new search is necessary ($\sigma_{\text{KF,ta}} > \tau_{\text{p}}$), and if so, the search can occur over a fraction of the 5 ns non-ambiguity range if $6\sigma_{\text{KF,ta}} < 5$ ns, greatly speeding up the process.

Synchronization

On initiation of synchronization, the time offset of the site B clock comb can suddenly change by up to the full 5 ns non-ambiguity range. As a consequence, the tracking comb at site A (the guide site) can lose acquisition and an entire re-acquisition cycle would need to be initiated. To avoid this issue, on initiation of synchronization site B transmits a short data packet by means of the digital communication channel indicating the size of the timing jump it is about to commit to its local clock comb along with the magnitude of the frequency error. When site A receives this packet, it temporarily pauses the active feedback to the site A tracking comb and instead implements exactly the same timing jump and timing slope in an open-loop manner. Once this open-loop time jump is completed, the site A tracking comb re-acquires the incoming clock comb but using a very short and restricted temporal search to account for any accumulated timing error during this open-loop operation either from atmospheric time-of-flight fluctuations or the relative reference oscillator drift. This restricted search is implemented by resetting the Kalman's filter's uncertainty to roughly 50 ps. After re-acquisition, site B is fully synchronized to site A, as shown by the out-of-loop verification.

Out-of-loop verification

The folded-link geometry used here allows for out-of-loop verification of the synchronization by measuring the relative timing of the pulses from the clock comb on site A and the synchronized clock on site B. The clock comb from site A was routed to site B by means of a fibre and combined with the synchronized clock comb on site B, filtered with a 12-nm wide filter at 1,560 nm, and detected on a balanced photodetector. The resulting signal is centred at the frequency offset between the two clock combs. The demodulated signal voltage depends on the relative timing between pulses. (Because there is no scintillation present, the full timing discriminator approach is not necessary.) The calibration between the demodulated voltage and the time offset of the clock combs is shown in Extended Data Fig. 6, which was generated by digitally stepping the offset applied to the synchronization feedback loop. For normal operation, we set the synchronization calibration offset so that zero-time offset falls at the half-way level so as to provide $maximum\,dynamic\,range\,for\,measurements\,of\,the\,out\text{-}of\text{-}loop\,timing.}$ From a fifth-order polynomial fit to the curve in Extended Data Fig. 6, we generate a calibration function that yields the out-of-loop time offset as a function of measured voltage.

Data availability

All data for the figures in this manuscript are available at https://data.nist.gov/od/id/mds2-2967.

Code availability

The algorithms necessary to perform this experiment are described between the main text and the Methods.

 Swann, W. C. et al. Low-loss reciprocal optical terminals for two-way time-frequency transfer. Appl. Opt. 56, 9406-9413 (2017).

Acknowledgements We acknowledge comments from T. Bothwell, F. Giorgetta and B. Washburn. We acknowledge technical assistance from S. Syed, M. Bodine, H. Leopardi, T. Wright, M. Martinsen, D. Kuniyuki, S. Baumann, the NOAA Mauna Loa Observatory and the Haleakala MEES Observatory. We acknowledge the Air Force Office of Scientific Research (grant no. MIPR F4FGA02152G001), Air Force Research Laboratory (grant no. FA9453-16-D-0004), NSF QLCI Award (grant no. OMA – 2016244), NSF GRFP (grant no. DGE 1650115), OSD and DARPA DSO through a CRADA with Vector Atomic and NIST for funding. Approved for public release: distribution is unlimited. Approval no. AFRL-2022-5993.

Author contributions J.-D.D., L.C.S. and N.R.N. conceived the experiment. E.D.C., J.-D.D., L.C.S. and N.R.N. acquired and analysed the synchronization data from Hawaii, and wrote the paper. J.-D.D. and H.B. developed the signal acquisition processing. J.E., E.D.C. and L.C.S. constructed the optical system and acquired 2 km data. W.C.S. and B.K.S. designed and built the free-space optical terminals and contributed to the writing.

 $\textbf{Competing interests} \ \mathsf{The \ authors \ declare \ no \ competing \ interests}.$

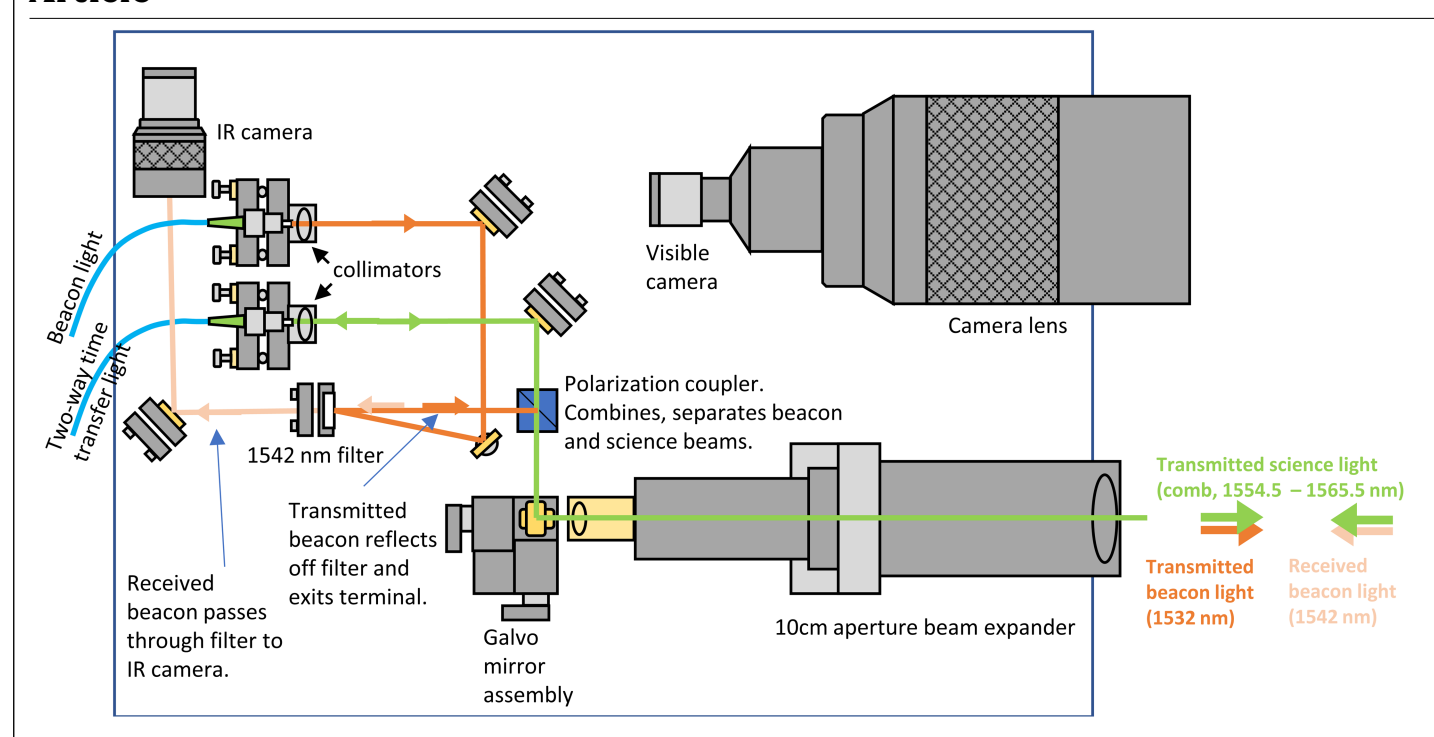
Additional information

Supplementary information The online version contains supplementary material available at https://doi.org/10.1038/s41586-023-06032-5.

Correspondence and requests for materials should be addressed to Nathan R. Newbury or Laura C. Sinclair.

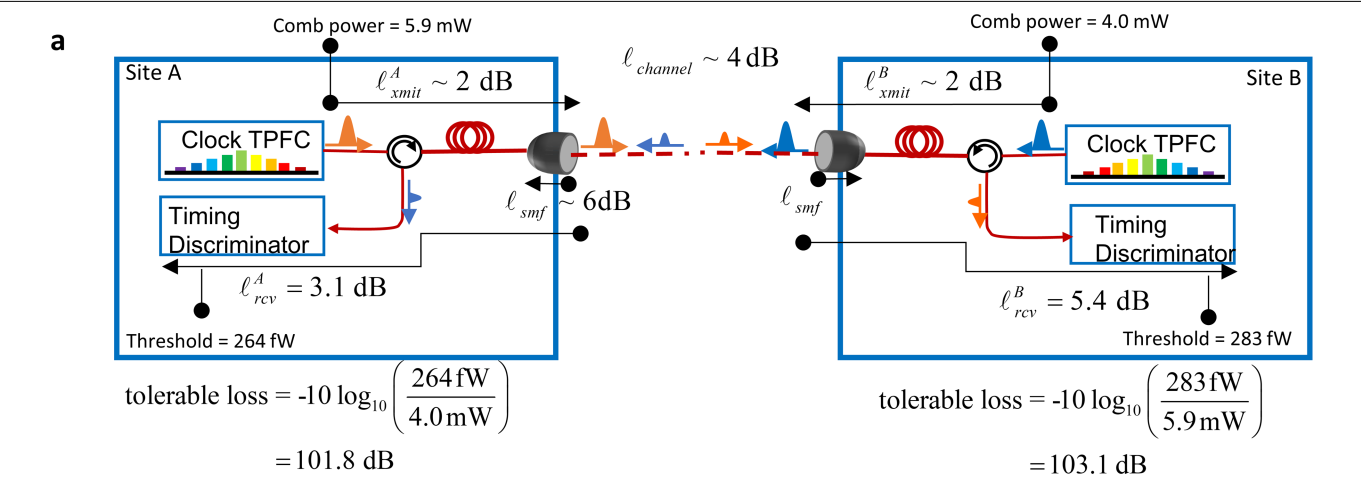
Peer review information *Nature* thanks David Gozzard and Jungwon Kim and the other, anonymous, reviewer(s) for their contribution to the peer review of this work. Peer reviewer reports are available.

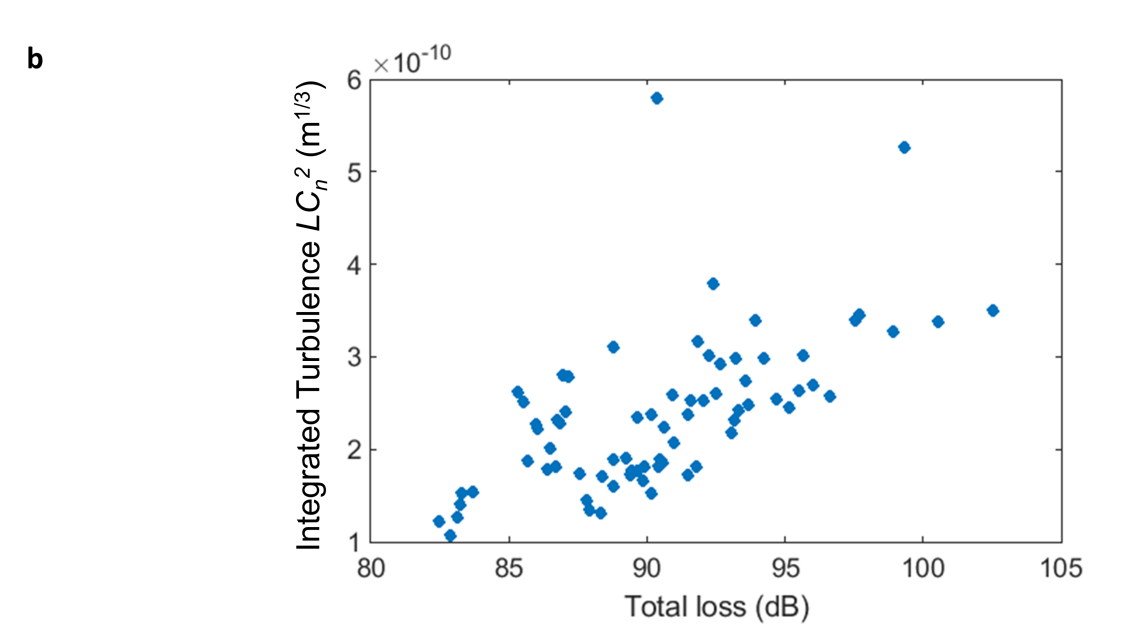
 $\textbf{Reprints and permissions information} \ is \ available \ at \ http://www.nature.com/reprints.$



 $\label{lem:extended Data Fig. 1 | Free space optical terminal design.} Each terminal transmits both the comb light (at a few mW) and a beacon laser signal at similar low power (-2 mW at the aperture) through a 10 cm aperture with an 8 cm <math>1/e^2$ beam diameter. To avoid sacrificing comb light to active tip/tilt stabilization, a separate beacon beam at 1532 nm or 1542 nm is polarization multiplexed directly onto the comb beam. (The beacon wavelengths differ for the two terminals, allowing wavelength demultiplexing of the transmitted and received beacon beams). A terminal's transmitted beacon beam, originating from a polarization maintaining fiber-coupled laser, is collimated through a

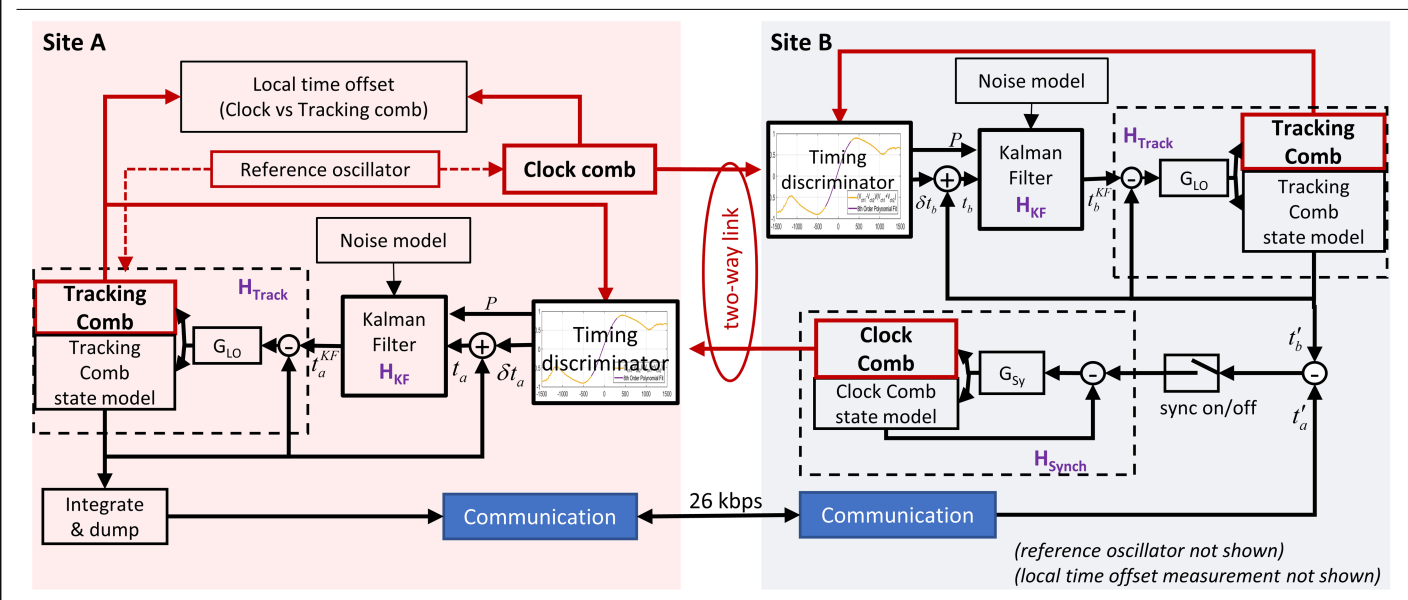
fiber collimator, reflected off the face of an interference filter (which acts as a mirror), and directed to the polarization coupler. The combined, -3.3-mm diameter beam is directed to a galvo mirror that provides tip/tilt control, and then passes through a 24:1,10 cm aperture beam expander. The beacon light is detected at the far end by a focal plane array. The images are processed, and the beam position fed back to adjust the tip/tilt of the outgoing combined comb light and beacon light. This corrects for atmospheric turbulence and optimizes coupling of the incoming frequency comb light into the polarization maintaining single-mode optical fiber.





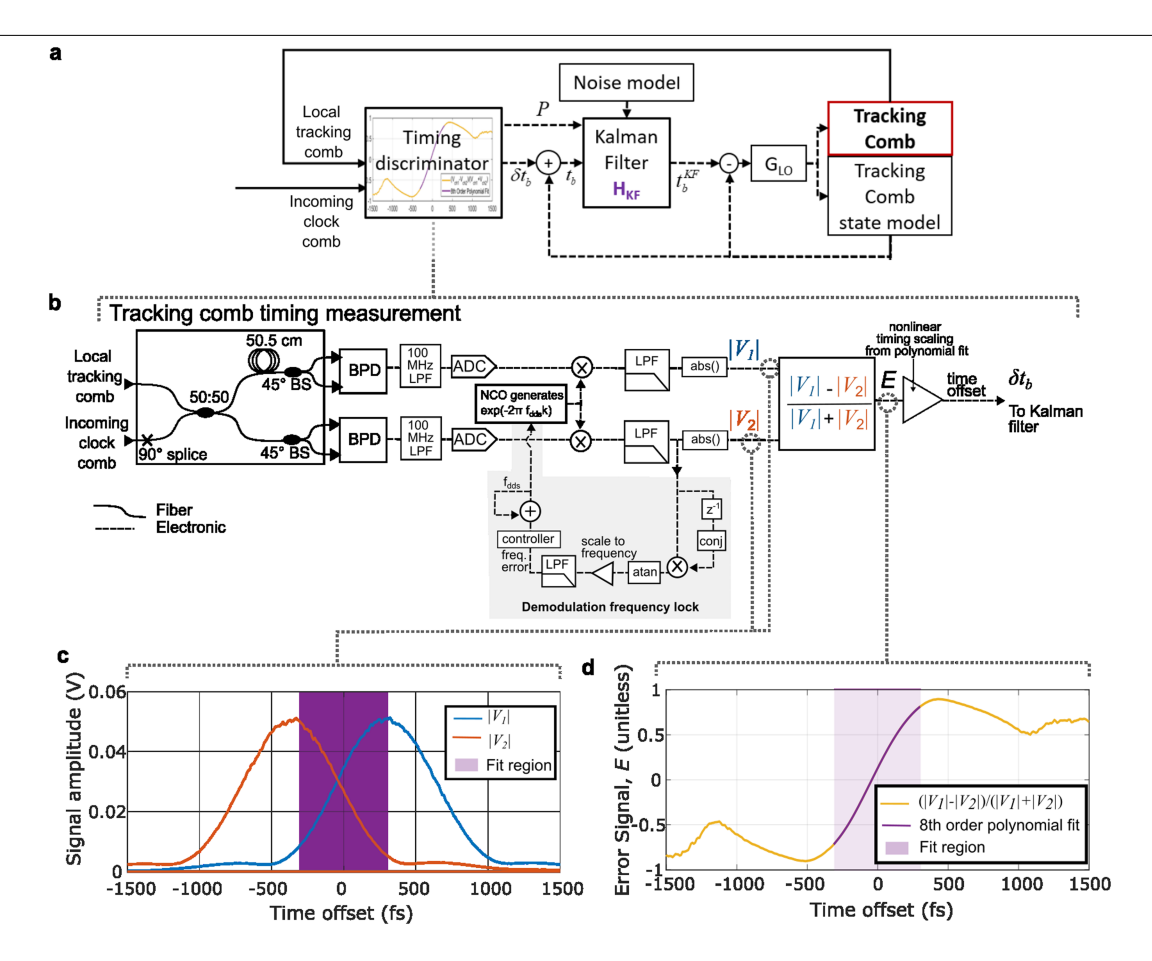
Extended Data Fig. 2 | **Total link loss.** (a) Diagram of link loss. The aperture-to-aperture link loss, which includes the channel loss $\ell_{channel}$, is reciprocal as is any excess loss from coupling into single-mode fiber, ℓ_{smf} , whereas the transceiver-specific losses ℓ_{rcv} and ℓ_{xmit} are not. While ℓ_{smf} is reciprocal for both sites, the loss is unidirectional, that is it only occurs when

the incoming light is coupled into the fiber. (b) Measured median total loss over different runs plotted against the integrated turbulence, as measured by the piston noise and assuming a wind velocity of 10~m/s. The mean loss across runs is 91~dB giving 11~dB margin over the tolerable loss of 102~dB.



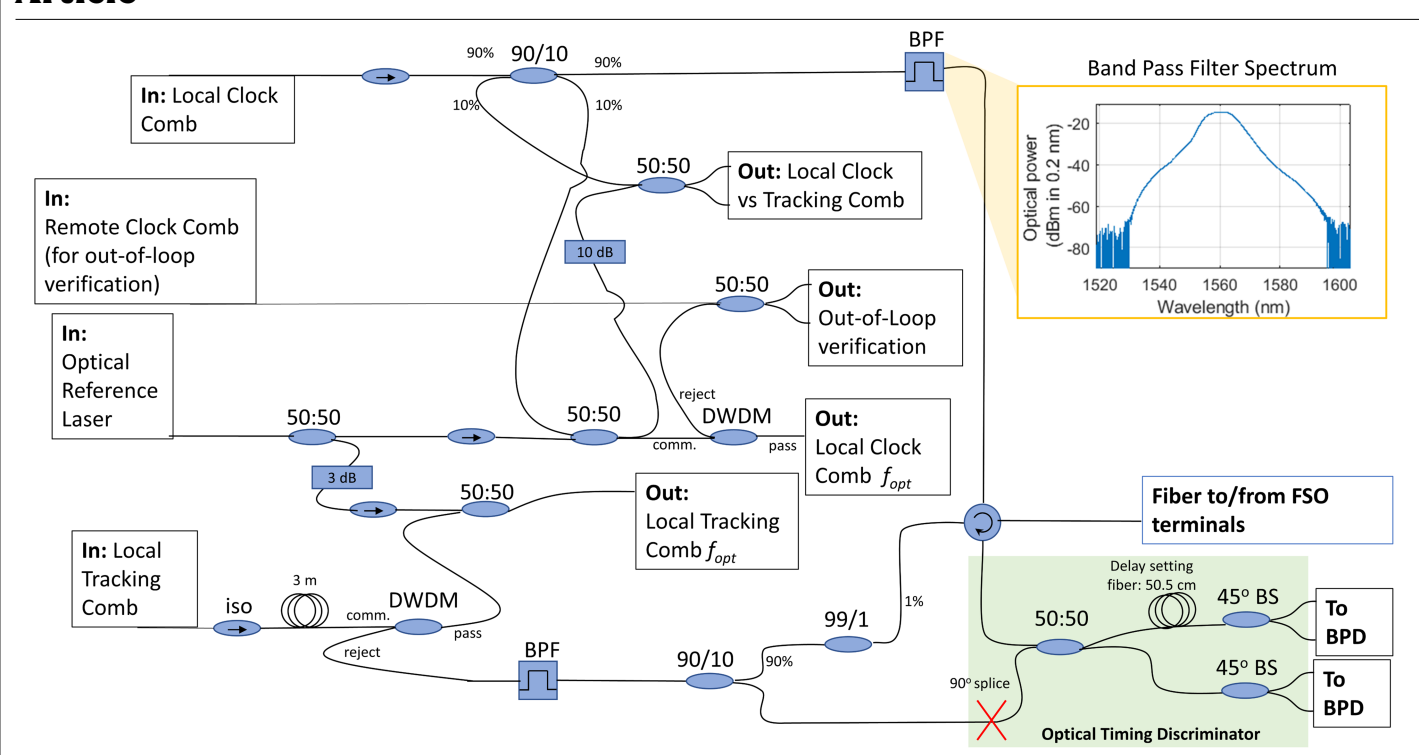
Extended Data Fig. 3 | System diagram emphasizing signal processing. Each site has a local reference oscillator (cavity stabilized laser), to which both the clock comb and tracking comb are self-referenced. As shown for site A, after both the clock and tracking combs are phase-locked to the reference oscillator, they have an arbitrary local time offset between each other. This local time offset is directly zeroed by digitally adjusting the tracking comb timing until there is a maximum heterodyne overlap with the clock comb pulses. $Subsequent \ timing \ values \ for \ the \ local \ tracking \ comb \ are \ then \ referenced \ to$ the local clock comb. After acquisition, the timing discriminator measures the (small) time offset δt_a between the incoming clock comb and local tracking comb. This timing difference is summed with the tracking comb time offset, to generate an estimate of the incoming clock comb pulse time, t_a . This estimate, along with the corresponding measured incoming power, is input to the Kalman filter, whose output provides an optimized, filtered estimate of the incoming clock comb pulse time, t_a^{KF} . This value is fed into a final feedback controller for the tracking comb, G_{LO} . Due to the feedback loop, the tracking comb output itself (both the physical optical pulse time and the corresponding

digital value), is now a filtered, estimated value of the incoming clock comb pulse timing with respect to the local clock comb pulse time. This value is transmitted over a communication link from site A to site B, where it is combined with the corresponding local value of t_h to generate an error signal for the site B clock comb. When both sites have acquired their lock onto the incoming clock comb pulses, the final synchronization feedback controller G_{sy} is activated and the site B clock comb is actively synchronized to the site A clock comb, at their local reference point. The effective bandwidth of the Kalman Filter depends on the input power, and ranges from 10 Hz to 25 Hz. The bandwidth of the subsequent lock of the tracking comb (H_{track}) is ~450 Hz. The bandwidth of the synchronization lock (H_{synch}) is ~15 Hz. The communication link is over rf coaxial cable here. For a future point-to-point link, it would be over free space by either rf or optical as in ref. 15. The message rate (for update of t_a) is 400 Hz and the total bit rate is 26 kbps. red solid lines: optical comb pulses, red dashed line: CW optical laser light, black lines: digital values, P: input optical power.



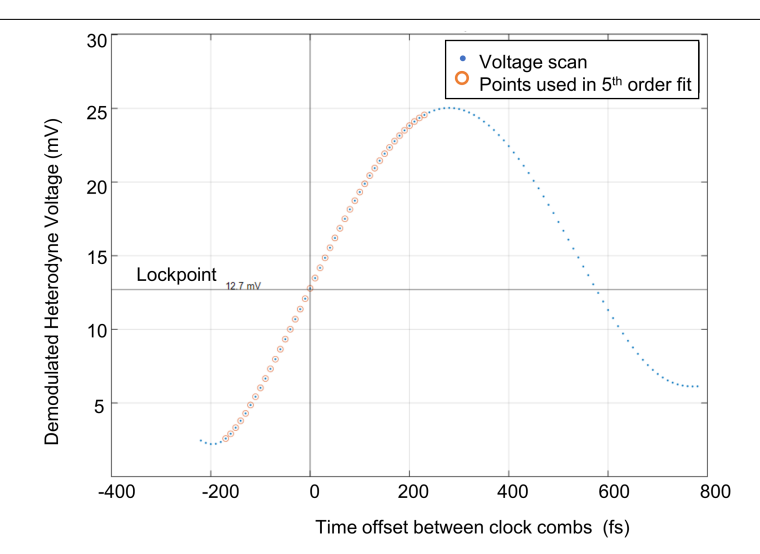
Extended Data Fig. 4 | Tracking comb timing measurement using an optical timing discriminator. (a) Subset of system diagram from Extended Data Fig. 4 showing how the timing of the incoming clock comb is measured with the local tracking comb. (b) System diagram of the optical timing discriminator and subsequent signal processing. The optical timing discriminator generates two measurement channels with the lead and lag positions between the two combs switched between channels. After measuring these channels on balanced photodiodes (BPD), the heterodyne output voltages are demodulated to generate IQ (complex) signals, which are then low pass filtered (LPF). The phase of one signal is used in a phase-locked loop to adjust the demodulation

frequency, f_{DDS} , and centre the baseband signals at DC. The magnitudes of the signals are combined to generate an estimate of the power (from their mean squared values) and a timing offset value, δt_b , from their normalized difference. BS, beam splitter; ADC, analog to digital converter; NCO, numerically controlled oscillator. (c) Absolute value of the timing discriminator output voltages, $|V_I|$ and $|V_2|$, as a function of the time offset between the local tracking comb and incoming clock comb. (d) The error signal generated from the two channels along with the polynomial fit used in the digital processing to generate the timing error value based on the normalized error signal, E.

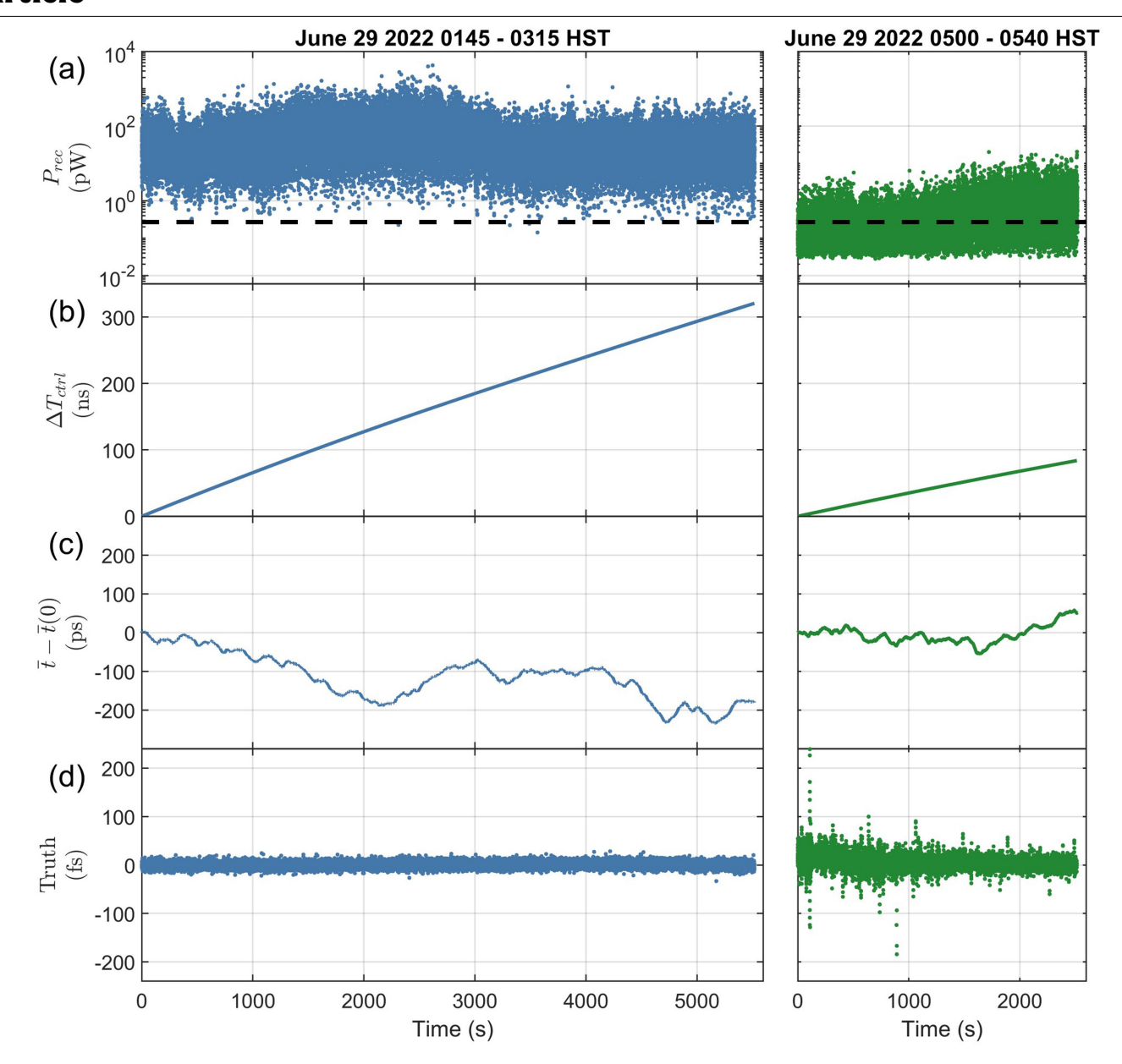


Extended Data Fig. 5 | **Optical time transfer transceiver design for a single site.** This transceiver routes the local clock comb to the FSO terminals and the incoming remote clock comb to the optical timing discriminator for mixing and detection with the local tracking comb. To minimize excess fiber optic delays, the transceiver also includes the necessary fiber optic components to generate the RF optical beat signals, f_{opt} , used for locking the two clock and tracking combs to the local cavity stabilized laser (CW in) reference, and the out-of-loop verification beat signals. The reference plane for the out-of-loop verification is defined by the point at which the two clock combs overlap within

the 50:50 splitter. A calibration step with a fiber-shorted link determines the time offset for the two clock combs due to path delays in the transceivers. This time offset is included in the overall synchronization loop so that the clock pulses remain overlapped when the system is operated over the link. All fiber is PM1550. 50:50, 50/50 splitter; 90:10, 90/10 splitter; BPF, band-pass filter; iso, isolator; DWDM, dense wavelength division multiplexer at the cavity-stabilized laser wavelength; 45° BS, polarization beam splitter with the input fiber rotated 45° .

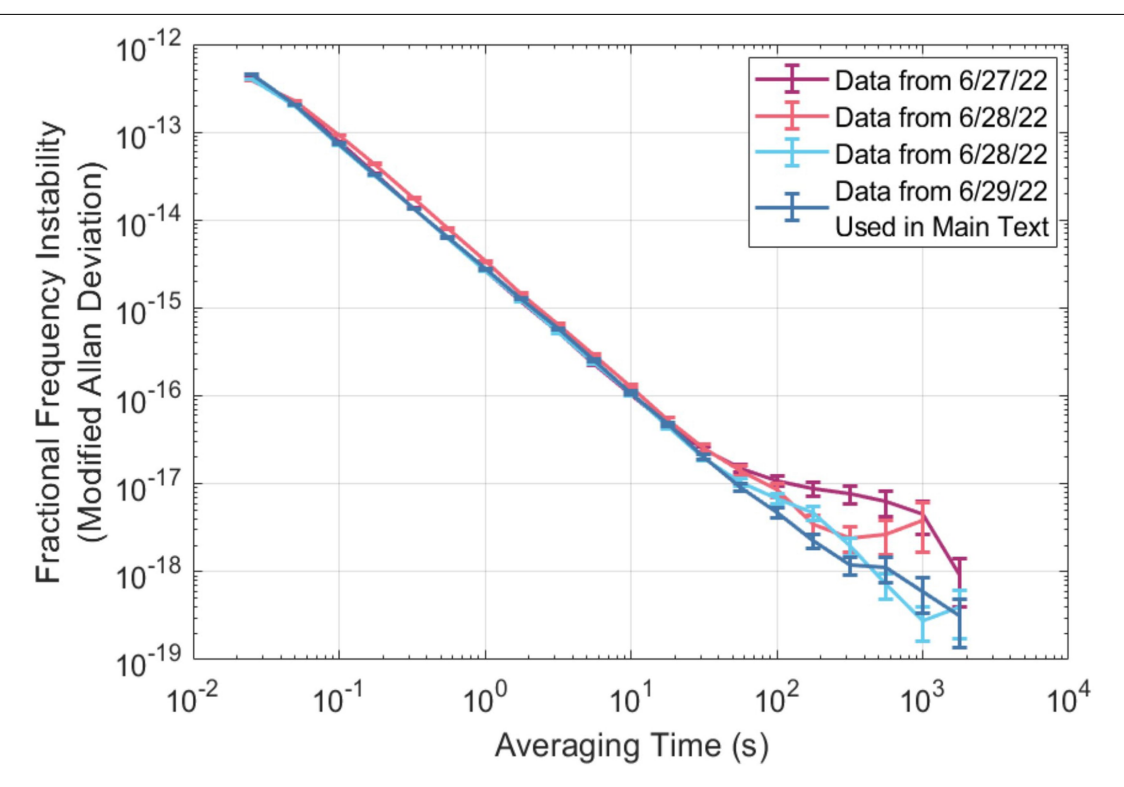


 $\textbf{Extended Data Fig. 6} | \textbf{Out-of-loop verification.} \ Calibration \ curve \ of \ heterodyne \ voltage \ vs \ time \ of \ set \ between \ the \ two \ clock \ combs \ used \ for \ out-of-loop \ verification. A \ fifth \ order \ polynomial \ is \ fit \ to \ the \ curve \ to \ generate \ a \ mapping \ from \ the \ measured \ demodulated \ heterodyne \ voltage \ to \ the \ time \ of \ fset.$

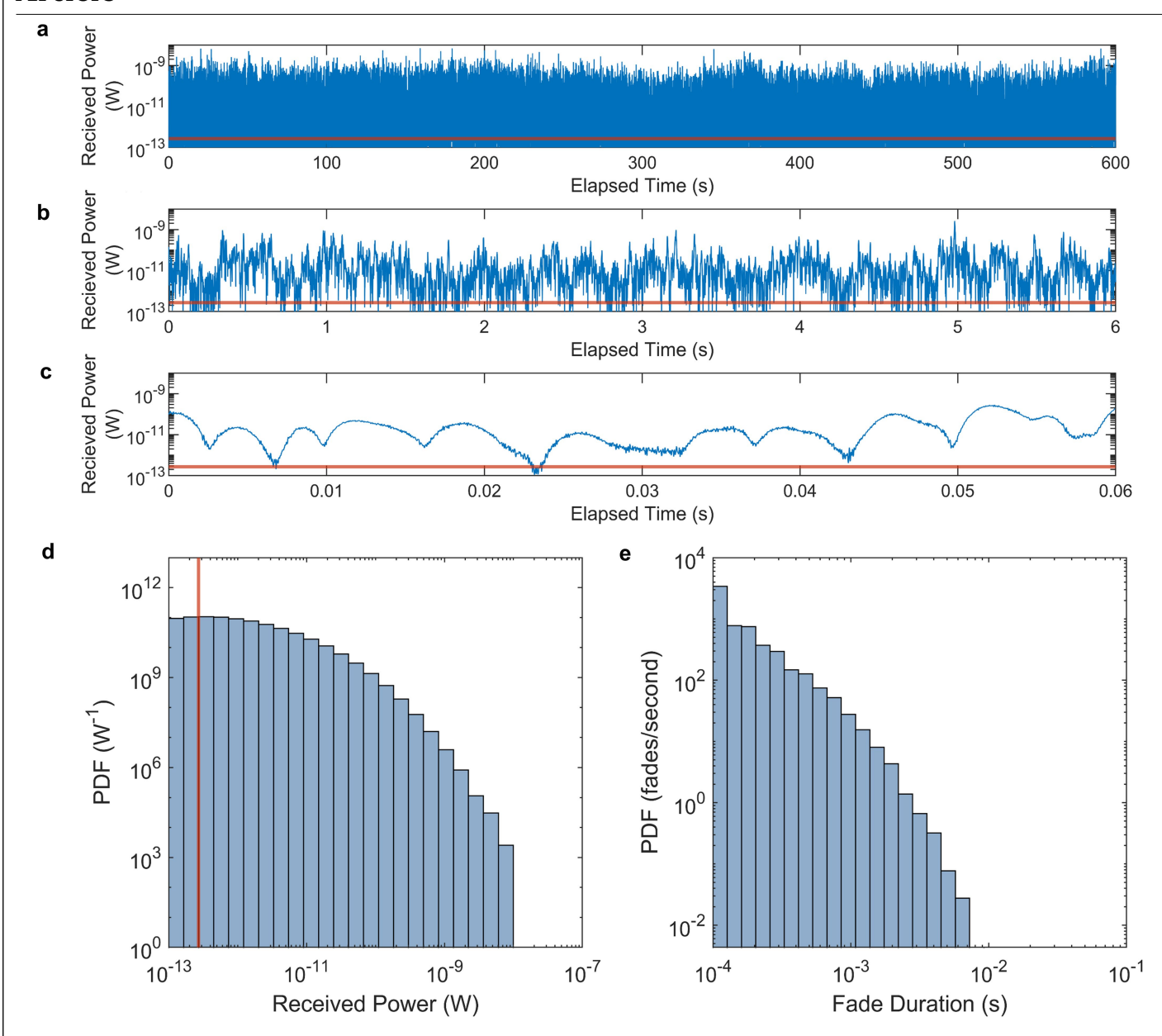


Extended Data Fig. 7 | Traces for synchronization over 300 km for 4.0 mW of comb power at site B (left, blue traces) and for reduced, 40 μ W comb power at site B (right, green curves). (a) Time trace of received power, P_{rec} , measured at the output of the timing discriminator for site A with the applied threshold shown as a dashed black line. (b) The control effort, ΔT_{cntrl} , applied on site B to maintain synchronization between the two site's clock combs. As such, it is also a measurement of the time offset between the two cavity-stabilized reference

lasers. (c) Changes in the time-of-flight. These changes are due to temperature drifts in the 300 km of air and in the fiber paths up to the terminals, atmospheric turbulence, and mechanical movement in the terminals. (d) The out-of-loop timing verification or 'Truth' data indicates constant temporal overlap between the clock combs at both sites despite 100's of ps changes in the time-of-flight and 100's of ns changes in ΔT_{cntrl} . This truth data is used to generate the instability deviations of Fig. 3.

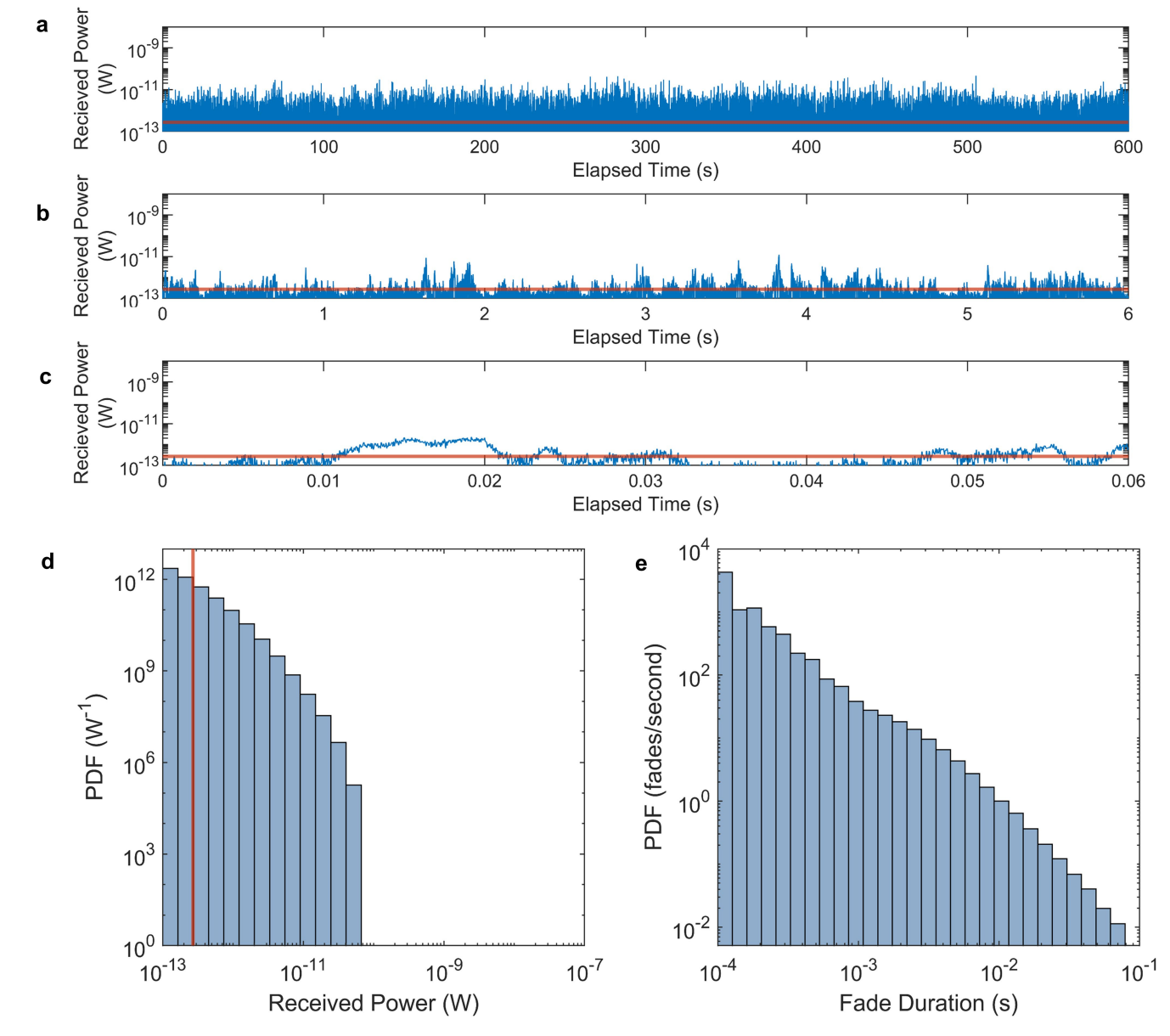


a malfunctioning temperature controller on the out-of-loop verification fiber and both transceivers. The data from June $29^{\rm th}$ (blue curve) also appears in Fig. 3 of the main text.



 $\label{lem:extended} \textbf{Extended Data Fig. 9} | \textbf{Received power and fade statistics over the 300 } km \\ \textbf{link at site A for 4.0 } mW of comb power from site B. (a-c) \\ \textbf{Received power over 600-seconds, 6 s, and 0.06 s. } Red \\ \textbf{line indicates the 270 } fW \\ \textbf{detection threshold. (d) } Normalized \\ \textbf{histogram (i.e., probability density function, PDF) } of \\ \textbf{or any other power forms of the probability density function, PDF) } of \\ \textbf{or any other power forms of the power forms of the probability density function, PDF) } of \\ \textbf{or any other power forms of the power forms$

the received power for the 600-second segment. (e) PDF of the fade durations. For the 4.0 mW comb power sent from site B, no fades exceeded a duration of 10 ms – a direct consequence of the low detection threshold at site A.



Extended Data Fig. 10 | Received power and fade statistics over the 300 km link at site A for 40 μ W of comb power from site B. (a-c) Received power over 600-seconds, 6 s, and 0.06 s. Red line indicates the 270 fW detection threshold. (d) Normalized histogram (i.e., probability density function, PDF) of the

received power for the 600-second segment. (e) PDF of the fade durations. For the greatly reduced launch power, fades are more frequency and of longer duration than the data of Extended Data Fig. 9.

$\textbf{Extended Data Table 1} \\ \textbf{Experimental parameters for the data in Figs. 2-4 related to quantum-limited operation} \\$

Quantity	Figure 2	Figures 3 and 4
	(square filters)	(Gaussian filters)
Pulse width for zero chirp, τ_p	245 fs	355 fs
Detector quantum efficiency, η	0.80	0.80
Detector noise penalty, D	1.2 (1.7 dB)	1.2 (1.7 dB)
Pulse broadening, C	1.35	1.7 (2-km link)
		1.5 (300-km link)
Quantum-limit, γ_{ql}	0.6	0.6
Actual γ	$2.1\gamma_{ql}$	$3.5\gamma_{ql}$ (2-km link)
		$2.7\gamma_{ql}$ (300-km link)

 $Pulse\ width\ is\ defined\ as\ the\ full-width\ half-maximum\ value.\ The\ values\ for\ C\ vary\ between\ sites,\ but\ the\ effective\ averaged\ value\ is\ provided\ here.$